Supplementary Information for: Simulating flow-induced reconfiguration by coupling corotational plate finite elements with a simplified pressure drag

Danick Lamoureux, David Melancon,* and Frédérick P. Gosselin†
Laboratory for Multi-Scale Mechanics (LM2), Department of Mechanical Engineering, Polytechnique Montreal, 2500 chemin de Polytechnique, Montreal (Quebec), H3T1J6, Canada

Sophie Ramananarivo
LadHyX, CNRS, École Polytechnique, Institut Polytechnique de Paris, 91120, Palaiseau, France
(Dated: November 26, 2024)

CONTENTS

I. NUMERICAL IMPLEMENTATION

A. Pressure field formulation - Development

The complete development of the pressure field formulation given in the main text is developed as follows. We use Reynolds' transport theorem to define the forces applied on a plate set at an angle θ.

$$\mathrm{d}F = \rho_f \vec{U}\left(\vec{U}\cdot\vec{n}\right)\mathrm{d}S = \rho_f \begin{bmatrix}0\\-U_\infty\end{bmatrix}\left(\begin{bmatrix}0\\-U_\infty\end{bmatrix}\cdot\begin{bmatrix}\sin\theta\\\cos\theta\end{bmatrix}\right)\mathrm{d}S = \rho_f U_\infty^2\begin{bmatrix}0\\\cos\theta\end{bmatrix}\mathrm{d}S. \tag{1}$$

This force $\mathrm{d}F$ being in the $\vec{x}-\vec{z}$ reference frame, we need to find the force in the local curvilinear reference frame $\vec{s}-\vec{n}$, such that $\vec{s}$ follows the plate in its plane and $\vec{n}$ is its normal. We therefore rotate the generated forces such that the normal dN and tangential dT forces are calculated as

$$dN = \frac{1}{2}C_D\rho_f U_\infty^2\cos^2\theta\mathrm{d}S \text{ and } dT = \frac{1}{2}C_f\rho_f U_\infty^2\cos\theta\sin\theta\mathrm{d}S, \tag{2}$$

where $\frac{1}{2}C_D$ and $\frac{1}{2}C_f$ are fitting parameters to account for aerodynamic effects that are not modelled here. We note however that the friction drag is typically considered negligible for the reconfiguration of these structures [1] at high Reynolds numbers and therefore $C_f \approx 0$, which leads to $T = 0$. We consider C_D as the drag coefficient of the equivalent

* david.melancon@polymtl.ca
† frederick.gosselin@polymtl.ca

rigid structure, so that the resulted drag of our reconfigurable structure can be compared to its rigid counterpart [2]. We consider the force distributed over the plate's area $\mathrm{d}S$ and find that the pressure on each infinitesimal element is

$$p = \frac{1}{2}\rho_f U_\infty^2 C_D \cos^2\theta. \tag{3}$$

Finally, while still considering our infinitesimal element of area $\mathrm{d}S$, its resulting drag needs to be rotated back into the $\vec{x} - \vec{z}$ reference frame such that

$$\mathrm{d}F = \frac{1}{2}\rho_f U_\infty^2 C_D \cos^3\theta \mathrm{d}S. \tag{4}$$

To obtain the drag of the overall structure, we integrate the drag of each infinitesimal element over our domain Ω as $D = \int_\Omega dF$.

B. Pressure field implementation

While applying a pressure load that varies with the angle the elements makes with the vertical axis on a face can be done in most commercial software, doing so in the current implementation requires applying pressure loads to singular nodes. However, a singular node does not make a specific angle with the reference coordinate system without its neighbouring surface adding context to the physical system. Therefore, to find the angle of the surface with the reference coordinate system at a specific node, a regression technique can be used. We first start by considering the deformed nodes from their reference position using their displacements Δu_i, Δv_i and Δw_i, with their deformed positions noted $[u_i\ v_i\ w_i]$. We define their position on the xy plane as $\vec{x}_i = [u_i\ v_i]^T$ and the transverse coordinate associated with this node as its value $f(\vec{x}_i) = w_i$. For a given node i, we consider all the nodes that share an element with this node i, which generates the list of connected nodes $Y = [\vec{x}_1\ \vec{x}_2\ \vec{x}_3\ ...]$ and the list of associated values $\vec{f}(Y) = [f(\vec{x}_1)\ f(\vec{x}_2)\ f(\vec{x}_3)\ ...]^T$. From there, we can calculate the plane that best fits through these nodes [3]

$$M^T M\vec{a} = M^T\vec{f}(Y), \text{ with } M = \begin{bmatrix}\mathbf{1} & Y^T\end{bmatrix}, \tag{5}$$

where $\vec{a}$ is a vector containing the coefficients of the plane. By calculating $\vec{a}$, we can find the expression of the plane as $a_0 + a_1 x + a_2 y = z$, which has a normal vector $\vec{n_i} = [-a_1\ -a_2\ 1]^T$. We find the angle this normal vector makes with the $xy-$plane, which is perpendicular to the z-axis noted as $\vec{z} = [0\,0\,1]^T$, by calculating

$$\theta_i = \arccos\left(\frac{\vec{n_i}\cdot\vec{z}}{||\vec{n_i}||||\vec{z}||}\right) = \arccos\left(\frac{1}{||\vec{n_i}||}\right). \tag{6}$$

Therefore, from the deformed nodes, we can calculate the angle the normal of the surface makes with the z-axis at every node's location and thus compute the local pressure load to apply on this node during the next iteration. Here, it makes sense to apply pressure loads to nodes, because the considered framework assumes linearly distributed pressures among the plates based on their nodal distribution [4]. We note that, for very large deformations, the pressure could reverse direction if the structure bends too much. To account for this problem, we calculate the undeformed normal and, if the dot product of the deformed normal and the underformed normal is not positive, we apply a zero-pressure load as this means the plate has reversed direction.

C. Software verification and validation

To ensure every part of the current software works properly, we proceeded to increasingly complex verification and validation cases.

Firstly, to ensure that the finite element assembler and element definition is correctly implemented, we study the small displacement of a unit plate (length $L = 1$ and width $W = 1$) under uniform transverse pressure. We note here that the specific units are not important, as long as they are consistent. We take inspiration from the "Reissner-Mindlin plate with Quadrilaterals" demonstration for FEniCS [5], which studies the displacement in the middle of a plate that is clamped all around subject to a uniform load. Bleyer [5] offers a theoretical solution to the problem, therefore allowing us to perform an adequate verification analysis. We use a Young's modulus $E = 1000$, Poisson's ratio $\nu = 0.3$, thickness $t = 10^{-3}$ and uniform dead load $p = t^3 = 10^{-9}$ oriented downwards. This test therefore also verifies the dead loads implementation. The theoretical solution given by the Kirchhoff-Love theory of plates gives $w = 1.381728443004 \times 10^{-05}$ [5], to which we compare the results of our simulations for different numbers of nodes

using a uniform Delaunay triangulation. We show in Fig. S1a a convergence analysis of the error according to the number of nodes and observe a slope of -1.0829. We know that a finite element framework using linear elements will converge at a rate $e = \mathcal{O}(h^2)$ and, in $2D$, $h \propto n^{-1/2}$ (as one doubles the number of nodes, the size of the elements will shrink by 4). Therefore, we should expect a convergence rate of $e = \mathcal{O}(n^{-1})$, which we observe. The finite element assembler and element definition therefore seem appropriately implemented, as we retain the finite element framework's convergence rate.

Secondly, we make sure that our Newton-Raphson implementation and follower loads are adequately implemented by repeating one of Caselli and Bisegna [4]'s tests. We consider a clamped-free slender beam under uniform follower load and solve for its deformation under varying pressure magnitudes. We choose the length $L = 10$, the Young's modulus $E = 1.2 \times 10^6$ and Poisson's ratio $\nu = 0$ as described by Caselli and Bisegna [4] and the width $W = 1$, the thickness $t = 1$, as it was not specified by Caselli and Bisegna [4] for this case. We also know $I = Wt^3/12$ for a beam of rectangular cross section. Once again, the units here are not relevant as long as they are coherent. All of the dimensions are presented in the inset of Fig. S1b, where the colors illustrate the magnitude of the displacement. We plot in Fig. S1b the force-displacement curve of the beam under follower load when considering both vertical and horizontal displacement, which show a highly nonlinear response. We see from Fig. S1b that our implementation obtains a perfect agreement with Caselli and Bisegna [4]'s, therefore showing that our implementation of their framework and of the Newton-Raphson nonlinear solver is correct.

Thirdly, since the capability of evaluating the current loads on the structure was not implemented by Caselli and Bisegna [4] in the distributed framework, therefore allowing displacement control, we implement it and verify it using another of their test cases. We consider the same beam as described previously, but instead of applying a pressure load upon it, we control its free end's vertical displacement while keeping it free to move in its horizontal plane. This is equivalent to applying a point load on its end, which was studied by Caselli and Bisegna [4]. The dimensions of this beam are, again, shown in the inset of Fig. S1c, where the colors illustrate the magnitude of the displacement. We once again plot the force-displacement curve in Fig. S1c when considering both horizontal and vertical displacements. From Fig. S1c, we once again observe perfect agreement between our solution and Caselli and Bisegna [4]'s. Therefore, when applying a displacement, we are also able to evaluate the equivalent load, allowing us to use displacement control.

Now that the basic elements of the finite element software are verified, we can supplement Caselli and Bisegna [4]'s implementation by adding unto it an arc-length solver. This allows the software to capture snap-back and snap-through instabilities. We use Kadapa [6]'s implementation of the arc-length solver and verify our implementation against one of their tests. We simulate two cylindrical roofs of length $L = 254\,\text{mm}$, radius $R = 2540\,\text{mm}$, half-aperture $\theta = 0.1\,\text{rad}$, Young's modulus $E = 3102.75\,\text{MPa}$ and Poisson's ratio $\nu = 0.3$, with one of them of thickness $h = 12.7\,\text{mm}$ and the other of thickness $h = 6.35\,\text{mm}$ using Kadapa [6]'s arc-length method implementation applied to Caselli and Bisegna [4]'s corotational framework. The dimensions are again shown in the inset of Fig. S1d and, as is typical with this benchtest, only a quarter of the structure is modeled due to the use of symmetries. We plot the force-displacement curves of both cylinders in Fig. S1d and observe that both cylinders observe a snap-through under load control, while the thinner cylinder observes a snap-back under displacement control. Therefore, our implementation of the arc-length method captures the snapping physics of these systems. Moreover, as shown in Fig. S1d, we see an excellent agreement between our numerical simulations and Kadapa [6]'s results, which indicate that we capture these physics accurately and that our implementation is adequate.

All the previous tests were made on theoretical and numerical predictions, but it is also interesting to observe if we can predict mechanical loads and instabilities observed experimentally. Therefore, before jumping into applying the fluid loading to our software, we validate it using an experimental tensile test of a kirigami sheet experiencing buckling [7], with the different dimensions illustrated in Fig. S1e. We use Isobe and Okumura [7]'s soft sheet defined by slits of length $L_s = 30\,\text{mm}$, horizontal spacing $d_x = 2.5\,\text{mm}$, vertical spacing $d_y = 5\,\text{mm}$ with 1 slit in its width ($N_x = 1$), leading to a width $W = 35\,\text{mm}$ and 21 slits in its length ($N_y = 10.5$), which leads to a length $L = 110\,\text{mm}$ ($100\,\text{mm}$ between the slits and we consider the width of one blade at both ends before the clamp). We simulate the beam when clamped at both ends and use displacement control to extend the sheet. We plot in Fig. S1e the force-displacement curve of this specimen and show, in the insets, the deformed shape of the specimen at different extensions. The colorscheme indicates the rotation angle of the blades with the axis perpendicular to the traction ($\vec{x}$-axis). We see here that the numerical force-displacement curve does not fit perfectly with the experimental data, but we observe similar slopes within the two ranges (in-plane traction regime and out of plane buckling [7]) and predict a similar extension for the transition between the two regimes. Therefore, it seems that the current finite element software predicts well reality and is therefore validated for solely mechanical loads.

Finally, now that the software is verified mechanically and a flow-induced reconfiguration simulation of the flat rectangular plate was made (see section III.A of the main text), we perform a convergence analysis on this flow-induced reconfiguration case. We use the same dimensions as the initial plate described in the main text. We simulate five different mesh sizes and use the finest two mesh sizes to generate a prediction of the theoretical result using Richardson's extrapolation [8]. We note that we use a small tolerance $\varepsilon = 10^{-12}$ for the Newton-Raphson

solver so that the error is due to the mesh and not the nonlinear solver's convergence. We study the convergence of our flow-induced reconfiguration software by using the Richardson extrapolation of the flat rectangular plate's reconfiguration number $\mathcal{R}$, vertical displacement w and horizontal displacement u at a Cauchy number $C_Y = 100$, as shown in Fig. S1f's inset. The Cauchy and reconfiguration number are both defined in the main text, and we define the normalized error as $|(\phi_{FEM} - \phi_{ref})/\phi_{ref}|$, where ϕ is the chosen value to study and the reference is Richardson's extrapolated data. In all these cases, we expect a logarithmic slope $k = 2$ and, in the case of adequate convergence, our different data points will fall unto the same respective lines. Richardson's extrapolation predicts convergence rates of 2.1248, 2.2285 and 2.1615 for the reconfiguration number, the horizontal displacement and the vertical displacement, respectively, which are close to the expected convergence rate. We therefore recover the results from the five differently refined simulations and plot the error according to the mesh size as shown in Fig. S1f. We see that the three arbitrary values we have decided to use follow the same trend and fall on relatively straight lines. Therefore, our flow-induced reconfiguration model has retained the finite element framework's convergence rate, although it encounters important nonlinearities using the pressure field formulation. Therefore, the finite element software is verified for both mechanical and fluid loadings, and is adequate to study more complex cases.

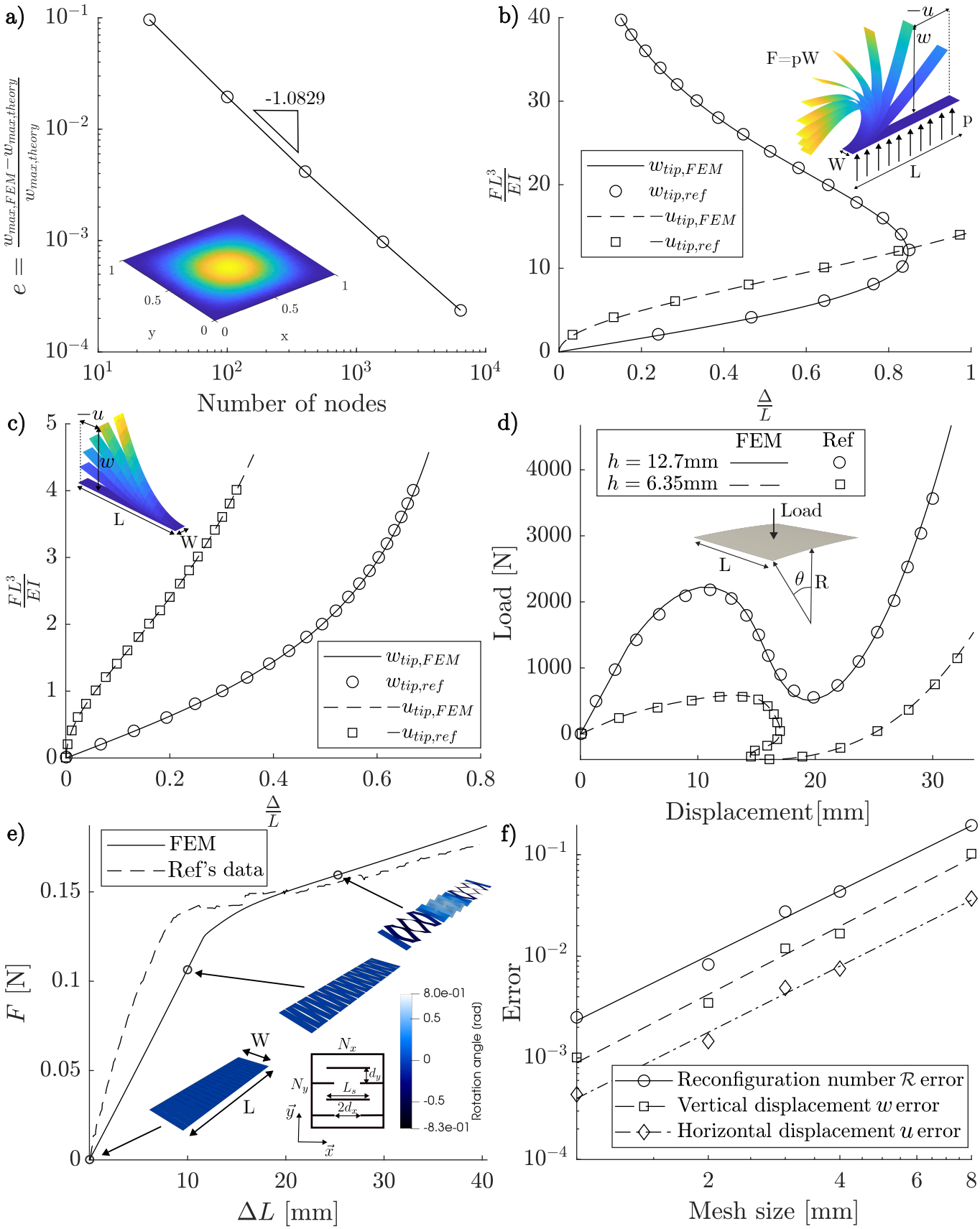

FIG. S1. **Verification and validation cases.** a) Convergence analysis of a unit plate under transverse loading. Reference is Bleyer [5]. b) Force-displacement curve of a beam under a uniform follower load. Reference is Caselli and Bisegna [4]. c) Force-displacement curve of a beam under displacement control of its free-end vertical displacement. Reference is Caselli and Bisegna [4]. d) Force-displacement curve of a cylindrical roof under a point load in its center observing snap-backs and snap-throughs. Reference is Kadapa [6]. e) Force-displacement curve of a kirigami sheet under traction. Experimental data from Isobe and Okumura [7]. f) Convergence analysis of the flow-induced reconfiguration of a flat rectangular plate.

II. THEORETICAL DEVELOPMENTS

A. Shading of the disk with multiple slits

We consider that the disk with multiple slits deforms axisymmetrically and neglect the discrete nature of the blades generated from the slits, therefore considering the structure continuous. Under these simplifications, the blades will shade evenly around the structure, causing the shading to be varied only radially, with no variation around the circumference. Therefore, while the applied pressure previously read

$$p = \frac{1}{2}\rho_f U_\infty^2 C_D \cos^2\theta, \tag{7}$$

with ρ_f the fluid density, U_∞ the flow speed, C_D the rigid structure's drag coefficient, and θ the plate's node's angle with the flow, we will need to add a term to account for this radial shading. We consider a ring around the undeformed disk at a radius R of infinitesimal width $\mathrm{d}R$. Once reconfigured, the ring will also be deformed and will now be at a radius $\tilde{R}$ of the center of the disk. We assume that the ring's undeformed area $2\pi R\mathrm{d}R$ stays the same and that, therefore, the deformed ring of area $2\pi\tilde{R}\mathrm{d}R$ is shading an area of $2\pi(R-\tilde{R})\mathrm{d}R$. We consider that the pressure due to the impinging flow should only be applied on the unshaded fraction of the disk $\tilde{R}/R$. The pressure applied on each node of the reconfigurable disk with multiple slits therefore reads

$$p = \frac{1}{2}\rho_f U_\infty^2 C_D \cos^2\theta \frac{\tilde{R}}{R}. \tag{8}$$

To compute the reconfiguration number under this new hypothesis, we adapt the method described in the main text such that

$$\mathcal{R} = \frac{\int_\Omega \mathrm{d}F}{\frac{1}{2}\rho_f U_\infty^2 C_D S} = \frac{\sum_{i=1}^{N_e} \frac{1}{2}\rho_f U_\infty^2 C_D \cos^3\theta_i S_i \frac{\tilde{R}_i}{R_i}}{\frac{1}{2}\rho_f U_\infty^2 C_D S} = \frac{\sum_{i=1}^{N_e} S_i \cos^3\theta_i \frac{\tilde{R}_i}{R_i}}{S}, \tag{9}$$

with R_i and $\tilde{R}_i$ the undeformed and deformed, respectively, mean radius of the i^{th} element.

III. ADDITIONNAL RESULTS

A. Disk with a single slit

To study the impact of shading and of contact, in flow-induced reconfiguration problems, we consider a disk with a single slit which rolls into a cone [9]. This disk, as shown in the insets of Fig. S2a, of external radius R_e and bending stiffness B, is pinned in its center on a radius R_i. Under a flow of density ρ_f and uniform velocity U_∞, with the drag of its rigid counterpart C_D, the disk will self-contact as it rolls into a cone with a tip angle that is more and more acute as the flow speed increases, therefore using both streamlining and area reduction mechanics. This geometry brings new phenomena not modeled in FIRM, i.e., shading area difficult to define and self-contact that leads to rolling and prevents interpenetration. In an ideal case, contact mechanics could be implemented into this software, but this adds another layer of nonlinearities and expensive computations to the finite element software as well as an important implementation complexity. Therefore, shading and contact mechanics are not implemented as they lie outside of the scope of the current paper, but we can still study the behavior of our simulated structure without these contributions. Schouveiler and Boudaoud [9] developed a model for this conically deformed disk that relies on the energy of a plate and on the axisymmetric deformation of the disk, which allows to explicit the Cauchy number C_Y, which they call their elastohydrodynamical number $\mathcal{N}$. Using this model, they find that the drag coefficient C_d of the flexible structure, which varies from the rigid structure's C_D, and the axisymmetric angle of attack α of the disk belong to master curves using the elastohydrodynamical number. We redefine the Cauchy number, based on their elastohydrodynamical number, as

$$C_Y = \frac{\rho_f U_\infty^2 C_D R_e^3}{B \ln(R_e/R_i)}, \tag{10}$$

and use the adapted reconfiguration number $\mathcal{R} = C_d/C_D$ in our study. The Cauchy number again represents the ratio of fluid load to elastic forces, and we now have two quantities to compare with: a measure of displacement α and a measure of applied forces $\mathcal{R}$.

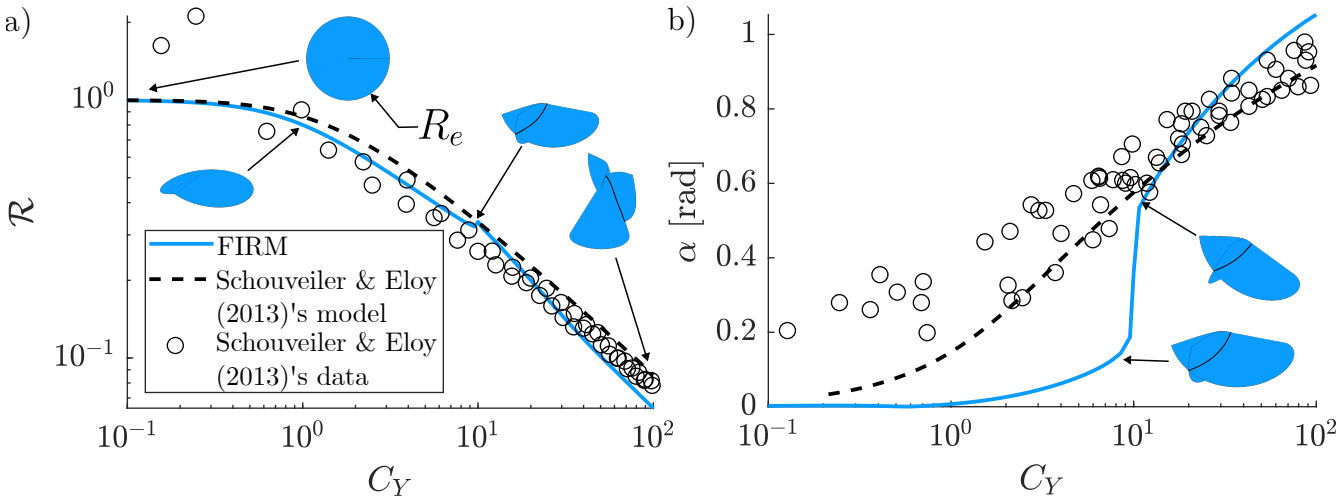

FIG. S2. **Flow-induced reconfiguration of a disk with a single slit.** a) Reconfiguration number $\mathcal{R}$ as a function of the Cauchy number C_Y and b) angle of attack α according to the Cauchy number C_Y for the disk with a single slit of external radius R_e, comparing the current implementation (FIRM) without shading or contact with Schouveiler and Boudaoud [9]'s model and experimental data. The insets of the different figures indicate the deformed structure at different Cauchy numbers.

We consider a disk similar to one of Schouveiler and Boudaoud [9]'s studied disks of external radius $R_e = 100\,\text{mm}$, pinned radius $R_i = 1\,\text{mm}$, thickness $t = 0.1\,\text{mm}$, Young's modulus $E = 23.04\,\text{GPa}$ and Poisson's ratio $\nu = 0.3$, leading to a bending stiffness $B = 1.92\,\text{N mm}$, for which its rigid counterpart has a drag coefficient $C_D = 2.0$. The disk is in a water channel of density $\rho_f = 997\,\text{kg m}^{-3}$ and velocity U_∞ oriented with the negative vertical axis $-z$, which is varied to obtain adequate Cauchy numbers $C_Y \in [10^{-1}, 10^2]$, and we use Eq. (6) like in the main text to compute the reconfiguration number. Once again, the exact dimensions are not critical, as long as they remain coherent. The angle of attack is calculated using the farthest node from the slit with its deformed position noted u, v, w such that

$$\alpha = \arctan\left(\frac{w}{\sqrt{u^2 + v^2}}\right). \tag{11}$$

We simulate the previously described case using our software without any corrections regarding shading or contact and obtain the $\mathcal{R}-C_Y$ and $\alpha-C_Y$ curves in Fig. S2a,b, respectively. We observe in Fig. S2a's insets that the disk does interpenetrate itself, as no contact mechanics are implemented. However, at high Cauchy numbers, we still observe the conical shape the disk rolls into. The plot in itself shows the reconfiguration number according to the Cauchy number, and we compare the results obtained from Schouveiler and Boudaoud [9]'s model and experimental data and our model. We compare with the experimental data to show that our model still follows closely the experimental results. We note that, while the disk does not roll into itself perfectly, the reconfiguration number remains similar to what is expected in the tested Cauchy number range. However, in comparison to what is observed for the flat plate and the disk with multiple slits in the main text, the transition between the different regimes is much smoother, while still present. Indeed, at low Cauchy numbers, the disk behaves like a rigid disk, while at high Cauchy number, we reach a constant Vogel exponent $\mathcal{V}$. As for Fig. S2b, we study the angle of attack according to the Cauchy number when comparing our model to Schouveiler and Boudaoud [9]'s model and experimental data. Experimentally, we see that the angle of attack increases smoothly according to the Cauchy number, which is captured by Schouveiler and Boudaoud [9]'s model. However, since our model does not capture shading nor contact, we observe an instability that causes the angle of attack to remain small until it grows to values that are within an acceptable range from the experimental results. Therefore, it seems that the angle of attack is predicted well at high Cauchy numbers, while the reconfiguration number is predicted well at low Cauchy numbers. The discrepancies observed in both Figures are assumed to be due to the lack of shading and contact, which causes the deformation to be non-physical.

B. Tensile test of a ribbon kirigami sheet

As discussed in the main text, we perform a traction simulation of a kirigami sheet similar to one of Marzin *et al.* [10]. To do this, we use the same procedure as performed for the verification test from Fig. S1e, with the sheet defined in the main text. Due to the larger number of degrees of freedoms, we stop the simulation early as each iteration takes

a long time and it requires small relaxations not to diverge. Therefore, we only reach an extension of 10 mm before stopping the simulation and measure the slope of the second linear regime. As mentioned in the main text, we find a stiffness of $K = 35.4\,\mathrm{N\,m^{-1}}$, where Marzin *et al.* [10] observed an experimental stiffness $K = 38.9\,\mathrm{N\,m^{-1}}$ for this specimen, which is in good agreement with what was observed numerically as we find an error of less than 10%. This error could come from experimental boundary conditions that are not exactly clamped, or slightly different material or geometrical properties than what is simulated. Nevertheless, we consider the current value acceptable for our use case.

C. Draping disk - Experimental results

Here we reproduced the experiments of Schouveiler and Eloy [11] to measure the drag loads on draping disks, which was not done previously. Moreover, we ran the experiments in a wind tunnel instead of a water tunnel. We used sheets of PolyEthylene Terephthalate (PET), also called Mylar, with varying thicknesses. This specific material also remains linearly elastic over a large range of strains [12]. We note, however, that plasticity effects might still play a role, which can be denoted by plastic deformations that are not recovered once reached, such as creases and folds in the sheets. Indeed, while performing different tests, we observed that Mylar can be plastically deformed if folds and creases are generated through deformation, which happens in modes 2F and above, as discussed by Schouveiler and Eloy [11]. The Mylar used has a Young's modulus of 4 GPa [10]. Our Mylar sheets come from a roll and therefore have an initial curvature that is removed by annealing [12] the Mylar sheets flat in an oven at 75 °C for an hour, ensuring precision and repeatability. This annealing procedure was applied before cutting any specimen. A CO2 cutter (EKO 7, THERMOFLAN) was used to cut our different specimens from different sheets. The manufactured specimens are described in the legend from Fig. S3a. We used an open section wind tunnel from the LadHyX at École Polytechnique with a square cross section of side-length 40 cm with a velocity range from 1.6m/s to 16m/s. A 6 axis force gauge (SIXAXES D65366 with balance type FX2.6 and 6 axis modular rack type RM6) is mounted downstream of the wind tunnel upon which a stand to hold our specimens can be mounted. The force gauge is tared under no flow so that the weight of the stand and the specimens do not alter the results. This way, only the specimen's drag will be monitored. In order to remove any transient effects from our analysis, we measure the forces on our specimens for 30 s at every flow velocity and use the mean of the axial force obtained.

Using the previously described setup, we performed the required wind tunnel tests. We first illustrate the different modes that can be obtained experimentally in Fig. S3a, such as modes C, $2F$ and $3F$. The velocity range and the specimens used did not allow us to reach sufficiently high Cauchy numbers to obtain mode $3F^*$ experimentally, as was recorded by Schouveiler and Eloy [11]. Specimens deforming in water might be more stable than in air. Nevertheless, we do encounter mode $2F$, which is not encountered numerically by Hua *et al.* [13], since they call mode C their mode $2F$. We assign a marker symbol to each deformation mode underneath it. The modes illustrated in Fig. S3a are shown in the sequence in which they were encountered experimentally as the flow velocity was increased.

We show, in Fig. S3b, the disks' drag D according to the flow velocity U_∞ when the flow velocity is increased. The different specimens are defined in the legend of Fig. S3a, where R is the external radius and t the thickness. We note that the clamp remains the same in all the experiments, with a clamp radius of $R_i = 6\,\mathrm{mm}$. We studied the drag from these disks such that both the thickness, and therefore the bending rigidity, as well as the external radius vary, therefore modifying all the parameters we can control in this case. The drag does not show an evident trend, other than stiffer and wider disks tend to generate more drag than more flexible, smaller disks, and that no two disks present exactly the same curves in their dimensional forms. Moreover, we note that we observe transitions from mode C to mode $2F$ and mode $2F$ to mode $3F$ using the symbols, and that these transitions also cause jumps in the drag curve, which are caused by snapping instabilities between the existing solutions. Indeed, as we increase the drag, we encounter mode C, which starts as a static reconfigured state [14], but soon starts fluttering. By increasing the flow velocity, the disk snaps into a mode $2F$ which is a sharp change from the fluttering mode C to a completely static mode $2F$. When uninstalling the disks that deformed in a mode $2F$ and $3F$, we notice plasticity creases around the clamp, similarly to what was observed by Schouveiler and Eloy [11, Supplemental material]. When we continue to increase the flow velocity, the disk transitions to mode $3F$, but in a smoother manner than previously. Moreover, while it was difficult for the disk to deform back into a mode C once they reached mode $2F$, it happened often for the disks to alternate between mode $2F$ and $3F$ when we remained around the critical transition velocity. To collapse the different curves unto master curves, we require to find the adequate dimensionless numbers, which is discussed in the main text.

Finally, we continued to measure the drag of our disks as we decreased the flow velocity, such that we could observe any existing hysteresis, or if multiple solutions exist for a single velocity, as shown in Fig. S3c, where the empty markers represent increasing velocities and filled markers represent decreasing velocities. We note that we only present the disks where we observe an hysteresis in order to reduce the visual load of the plot. We notice that once the disk reach

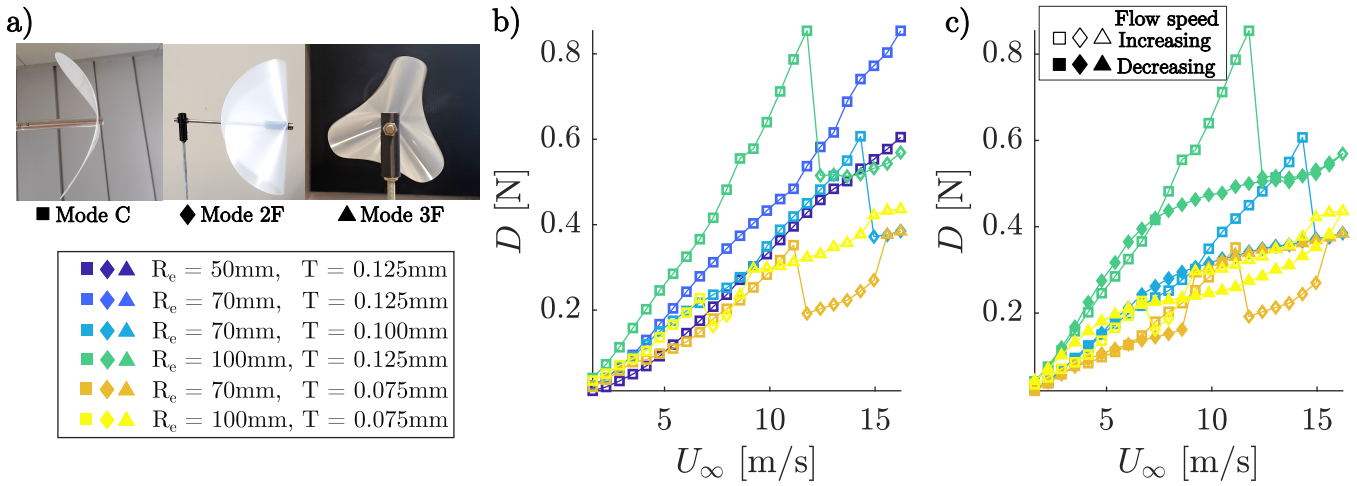

FIG. S3. **Experimental results regarding the drag of the draping disk.** a) Deformation modes of the disks under reconfiguration. Mode C bends symmetrically and is assigned a square marker. Mode $2F$ generates two creases symmetrically which causes it to fold and is assigned a diamond marker. Mode $3F$ has a third crease in comparison to mode $2F$, folding another time. Mode $3F$ is assigned a triangle marker. A legend of the different specimens that were tested is shown underneath with the used colorscheme and dimensions. b) Drag - velocity curve of the different specimens when the velocity is increased. c) Drag-velocity curve during flow-speed increase and decrease of the specimens which showed a deformation hysteresis.

mode $2F$ and higher, they tend to remain in this deformed state when decreasing the flow velocity. This is potentially due to the plasticity creases mentioned earlier [11], but also to the complex snapping instabilities observed. This leads to important drag discrepancies when increasing and decreasing the flow, as modes $2F$ and $3F$ tend to generate higher drag loads at low Cauchy numbers than mode C.

[1] A. Bhati, R. Sawanni, K. Kulkarni, and R. Bhardwaj, Role of skin friction drag during flow-induced reconfiguration of a flexible thin plate, Journal of Fluids and Structures **77**, 134 (2018).
[2] F. Gosselin, E. de Langre, and B. A. Machado-Almeida, Drag reduction of flexible plates by reconfiguration, Journal of Fluid Mechanics 10.1017/S0022112009993673 (2010).
[3] C. Audet and W. Hare, *Derivative-Free and Blackbox Optimization* (Springer, 2017).
[4] F. Caselli and P. Bisegna, Polar decomposition based corotational framework for triangular shell elements with distributed loads: COROTATIONAL FRAMEWORK WITH DISTRIBUTED LOADS, International Journal for Numerical Methods in Engineering 10.1002/nme.4528 (2013).
[5] J. Bleyer, *Numerical Tours of Computational Mechanics with FEniCS* (2018).
[6] C. Kadapa, A simple extrapolated predictor for overcoming the starting and tracking issues in the arc-length method for nonlinear structural mechanics, Engineering Structures 10.1016/j.engstruct.2020.111755 (2021).
[7] M. Isobe and K. Okumura, Continuity and discontinuity of kirigami's high-extensibility transition: A statistical-physics viewpoint, Physical Review Research 10.1103/PhysRevResearch.1.022001 (2019).
[8] Procedure for Estimation and Reporting of Uncertainty Due to Discretization in CFD Applications, Journal of Fluids Engineering **130**, 10.1115/1.2960953 (2008).
[9] L. Schouveiler and A. Boudaoud, The rolling up of sheets in a steady flow, J. Fluid Mech. 10.1017/S0022112006000851 (2006).
[10] T. Marzin, K. Le Hay, E. de Langre, and S. Ramananarivo, Flow-induced deformation of kirigami sheets, Physical Review Fluids 10.1103/PhysRevFluids.7.023906 (2022).
[11] L. Schouveiler and C. Eloy, Flow-Induced Draping, Physical Review Letters 10.1103/PhysRevLett.111.064301 (2013).
[12] T. Marzin, *Flow-gamis : Interaction of folds and cuts with a flow*, Ph.D. thesis (2023), thse de doctorat dirige par Langre, Emmanuel de Ingnierie, mcanique et nergtique Institut polytechnique de Paris 2023.
[13] R.-N. Hua, L. Zhu, and X.-Y. Lu, Dynamics of fluid flow over a circular flexible plate, Journal of Fluid Mechanics 10.1017/jfm.2014.571 (2014).
[14] M. Boukor, A. Choimet, . Laurendeau, and F. P. Gosselin, Flutter limitation of drag reduction by elastic reconfiguration, Physics of Fluids **36**, 021915 (2024), https://pubs.aip.org/aip/pof/article-pdf/doi/10.1063/5.0193649/19702290/021915_1_5.0193649.pdf.